Check for updates

Natural iron embedded hierarchically porous carbon with thin–thickness and high-efficiency microwave absorption properties†

Can Zhang,‡[a] Kuihu Zhao,‡[a] Xueai Li, [ID] *[a] Wenqi Dong,[a] Sufeng Wang,[a] Yunchun Zhou[b] and Haiyan Wang [ID] *[a]

The traditional strategy for fabricating transition metal/carbon composite microwave absorbing materials (MAMs) is to combine different metallic salts and carbon precursors *via* various techniques, in which raw material waste and environmental pollution are inevitable. In this work, without addition of any metallic salts, natural iron embedded hierarchically porous carbon (HPC) composites are synthesized for the first time *via* facile pyrolysis and subsequent "reductive activation" with KOH. Using KOH to react with carbon to generate H_2 can not only generate abundant nanoscale structures in the composites, but also *in situ* reduce the natural iron present in the bio-precursor to Fe nanoparticles, which facilitates the interfacial polarization and conductive loss of samples considerably. In turn, the modulation of graphitization degree could be realized by simply adjusting the ingredient ratio. Due to the synergistic effect between porosity and graphitization degree, the impedance matching of composites can be well regulated. The reflection loss of HPC-1 achieves −53.6 dB and the effective absorption bandwidth can cover the whole X and Ku bands with a thickness of only 1.4–2.4 mm. This study may pave a way to research on using bio-precursors rich in iron to synthesize high-efficiency and thin–thickness microwave absorbers and promote the diversified development of bio-derived materials in a gentle and facile way.

1. Introduction

Currently, the serious electromagnetic radiation caused by the rapidly developing wireless communication technology and radar devices has posed a nonnegligible threat to both the physical health of human beings and national information security.[1–5] For this reason, two categories of functional materials, *i.e.*, electromagnetic shielding materials and microwave absorbing materials (MAMs), have been investigated and fabricated by researchers worldwide for defending people and electronic equipment from this undesirable harm.[6–8] In particular, MAMs, which can efficiently dissipate microwaves by means of converting the electromagnetic energy to thermal energy, play a vital role in solving these problems.[9–11] Out of practical application needs, the state-of-art microwave absorbers are required to be thin in thickness, broad in effective absorption bandwidth, light in weight and strong in reflection loss (RL). As a kind of typical MAM, carbonaceous materials such as carbon nanotubes,[12] graphite,[13] and porous carbon[14,15] possess the advantages of natural abundance, excellent physiochemical properties, light-weight and good corrosion resistance. Porous carbon, especially hierarchically porous carbon (HPC), is generally considered to be a fabulous candidate with great prospect of wide development and application for microwave absorbers due to its low density as well as large specific surface area. Moreover, the hierarchically porous architecture has been proven to have a huge contribution on the attenuating ability for microwave absorbers. Wu *et al.* reported that the HPCs possess stronger absorption efficiency and broader bandwidth than ones with or without an uniformly porous architecture due to the superimposed positive effects of multiscale pores.[16] In specific, nanoscale pores are favor of bringing about interfacial polarization when being exposed to microwave, while micro-scale pores could extend the transmission paths for incident microwave in the interior of carbon matrix.

Conventionally, there are two approaches to fabricate porous carbon: artificial templet and biomass-templet method. Compared with biomass-templet method, the traditional artificial templet strategy, including "hard template" and "soft template" methods, is much more complicated and sometimes

[a]*Hebei Key Laboratory of Applied Chemistry, Hebei Key Laboratory of Heavy Metal Deep-remediation in Water and Resource Reuse, College of Environment and Chemical Engineering, Yanshan University, Qinhuangdao 066004, P. R. China. E-mail: lixueai@ysu.edu.cn; hywang@ysu.edu.cn*

[b]*National Analytical Research Center of Electrochemistry and Spectroscopy, Changchun Institute of Applied Chemistry, Chinese Academy of Sciences, Changchun 130022, P. R. China*

† Electronic supplementary information (ESI) available. See DOI: 10.1039/d0ra07963d

‡ These authors contributed to the work equally and should be regarded as co-first authors.

even environmentally unfriendly.[17,18] On the other hand, the biomass-templet method that utilizes reproduceable biomasses such as residues of vegetable,[19] wood,[20] rice husk ash[21] and so on as carbon sources to produce biomorphic functional porous carbon-based absorbers has unparalleled advantage on cost reduction, and meanwhile is of great significance to make the wastes profitable. For instance, Qiu *et al.* utilized the walnut shell as carbon source to prepare nano-porous carbon, and the minimum RL reached up to −42.4 dB when the thickness of absorber is 2.0 mm;[22] Zhou *et al.* used fish skin as carbon precursor to synthesize three-dimensional carbon foam *via* hydrothermal and pyrolysis process, whose reflection loss reached −33.5 dB with a thickness of 3.0 mm;[23] Wu *et al.* prepared HPC by one-step carbonization of spinach, which displayed the strongest RL of −62.2 dB at a thickness of 2.71 mm.[24] Although these porous carbon based-MAMs exhibit impressive absorptivity, the requirement of thin thickness can hardly be fulfilled by them due to their limited loss mechanism. For the purpose of enriching the loss mechanism of carbonaceous absorbers, the typical method is to combine together different heterogeneous components with them *via* various techniques, which mostly are transition metals or their oxides. For example, Wang *et al.* prepared jute-derived Fe_3O_4/C composites *via* pyrolysis and chemical coprecipitation, and the RL of −35.5 dB was realized at a thickness of 1.6 mm.[25] Nonetheless, it should be noted that some biomasses rich in transition metal Fe were utilized to synthesize porous carbon with the advantage that the native iron can serve as natural catalyst to modify the microstructure of carbon.[26] Such an interesting finding is supposed to have huge potential in microwave absorption, however, there are few relevant reports. In this work, a high-performance natural iron embedded HPC was fabricated *via* pyrolysis and subsequent reductive activation of discarded brine shrimp eggshells (BSES). Brine shrimp, which is a member of the crustacean subphylum and mainly live in coastal waters, salt ponds and plateau salt lakes, is usually hatched for aquaculture feed, however, BSES are disposed of as waste. Through reductive activation with potassium hydroxide (KOH), not only abundant nanostructures were produced in the carbon framework, but also a number of Fe nanoparticles were *in situ* reduced from the iron already present in BSES by the H_2 gas generated from the reaction between KOH and carbon. In turn, the graphitization degree could be modulated by adjusting the ingredient ratio simply. Due to the synergistic effect between porosity and graphitization degree, the impedance matching of composites can be well regulated by means of adjusting dosage of KOH. In addition, by using BSES as precursor, the naturally contained N and O elements in chitosan and amino acids would lead to the formation of the heteroatoms *in situ* doped carbon during pyrolysis, which could bring a positive contribution on the polarization ability of the material. Therefore, the as-prepared HPCs embedded with natural iron present optimum performance of a minimum RL of −53.6 dB with a filler loading of 20%, and an effective bandwidth covering both the X and Ku bands with the thickness from 1.4 to 2.4 mm. Compared with the previous procedures involved with hydrogen introduction or impregnation with

ferric salts,[25,27] this work attaches more significance to utilizing the bio-precursor with abundant iron content to fabricate novel Fe/carbon MAM for promoting the diversified development of microwave absorbers towards a much gentler and more facile direction.

2. Experimental section

2.1 Raw materials

BSES were provided by Chinese Academy of Fisheries Science. Potassium hydroxide (KOH, guaranteed reagent) was purchased from Shanghai Maclin Biochemical Technology Co., Ltd. (Shanghai, China). Hydrogen nitrate (HNO_3, analytical purity, 65.0–68.0 wt%) were bought from Xilong Chemical Industries Co., Ltd. (Guangzhou, China). All chemicals were used without further purification.

2.2 Preparation of natural iron embedded HPCs

First, the raw BSES were washed with deionized water and ethanol for several times to remove obvious impurities. Subsequently, the dried BSES were transferred into a quartz boat and calcined at 300 °C for 3 h for getting rid of the volatiles, and then heated to 700 °C with a heating rate of 1 °C min^{-1} under an argon atmosphere and held at that temperature for 4 h in a tube furnace. Furthermore, the product was cooled to room temperature, immersed in 67 wt% HNO_3 (20 mL), washed to neutral and then dried, which is eventually marked as C-700. Subsequently, C-700 was uniformly mixed with KOH at weight ratio of 1 : 0.5, 1 : 1, and 1 : 2 by a mortar. Similarly, the mixture was heated to 700 °C under an argon atmosphere at a heating rate of 10 °C min^{-1} and maintained at this temperature for 1 hour. Last, the resultant products were washed with deionized water until neutral, followed by drying in an oven at 80 °C. The as-prepared samples were correspondingly denoted as HPC-0.5, HPC-1, and HPC-2.

2.3 Characterization

Field emission scanning electron microscope (FESEM) images were taken by HITACHI S-4800. Transmission electron microscope (TEM) and high-resolution transmission electron microscope (HRTEM) images were obtained from HITACHI HT7700 electron microscope and FEI Tecnai G2 F20 electron microscope, respectively. X-ray diffraction (XRD) spectra were recorded from Rigaku D-max-2500/PC X-ray diffractometer. Thermogravimetric (TG) analysis was performed on NETZSCH STA 449 F5. Nitrogen adsorption–desorption isotherms were obtained using a Quantachrome Autosorb-1 apparatus under 77.4 K. X-ray photoelectron spectroscopy (XPS) test was carried out by ESCALAB 250Xi with a Al-Kα exciting source. Inductively coupled plasma-atomic emission spectrometry (ICP-AES) was performed on Agilent 5110. Raman spectra were collected by Renishaw inVia under a Raman microscope equipped with a He–Ne laser source (λ = 532 nm). Agilent N5234A vector network analyzer (VNA) was used to acquire the relative complex permittivity and permeability of samples. In order to prepare the test samples, the powder product was firstly mixed with

paraffin at a weight fraction of 20%, and then pressed into a ring with an outer diameter of 7.00 mm and inner diameter of 3.04 mm.

3. Results and discussion

In order to determine the pyrolysis procedure, TG analysis was exploited to obtain a pyrolysis profile of BSES. As shown in Fig. S1,† the TG curve recorded under Ar presents two abrupt decline stages from the temperature of 25 °C to 750 °C. The initial weight loss (~20%) below 150 °C is mainly owing to the removal of moisture and volatile impurities, and the significant weight loss (~53%) from approximately 220 °C to 700 °C corresponds to the degradation process. It's notable that the temperature of approximately 300 °C is an important period in which glycerol and proteins decompose. Accordingly, the raw BSES were heated to 300 °C first and held there for 3 h, and then heated to 700 °C and held there for 4 h.

FESEM was employed to investigate the morphologies of samples. As displayed in Fig. 1a, the raw BSES present an inborn multilayer porous structure, and this unique porous structure is well-preserved after pyrolysis and activation (Fig. 1b, c and S2†). By right of the basically preserved porous architecture, the pore-size distribution of HPC-1 was statistically surveyed in terms of FESEM (Fig. 1c) and TEM (Fig. S3a†) images. As illustrated in Fig. 1d, the pores within the statistical range possess

a submicron/micron size distribution from 50 nm to 2.39 μm, and the mean size is 0.50 μm.

TEM and HRTEM were further utilized to investigate the detailed microstructure of the as-prepared HPCs. As shown in Fig. 2a and S3b,† plenty of Fe nanoparticles are successfully *in situ* reduced from the natural iron inherited from BESE, and distribute uniformly in the carbon matrix. The high-magnification TEM image of the carbon skeleton in Fig. 2b reveals that numerous nanoscale porous structure were produced *via* activation with KOH. Furthermore, the image in Fig. 2c taken from the edge of the carbon shows that the carbon arranges into layered agglomerates with short range-order, indicating its moderate graphitization degree. Additionally, the HRTEM images show that the Fe nanoparticles are closely embedded in the carbon matrix, which forms heterogeneous interface, and present a crystal face with a lattice spacing of 0.20 nm corresponding to (1 0 0) plane of α-Fe, as shown in Fig. 2d and S3c.† The results of corresponding element mappings (Fig. 2f) manifest that the as-fabricated HPCs are rich in N and O elements in addition to Fe, suggesting that N and O atoms inherited from chitosan and amino acids are successfully *in situ* co-doped into the carbon hexagons and present a quite homogeneous elemental distribution.

The crystal phases of BSES and HPCs were characterized *via* XRD. As shown in Fig. S4a,† the raw BSES present three diffraction peaks at $2\theta = 20.8°$, $26.6°$, and $50.1°$, which are
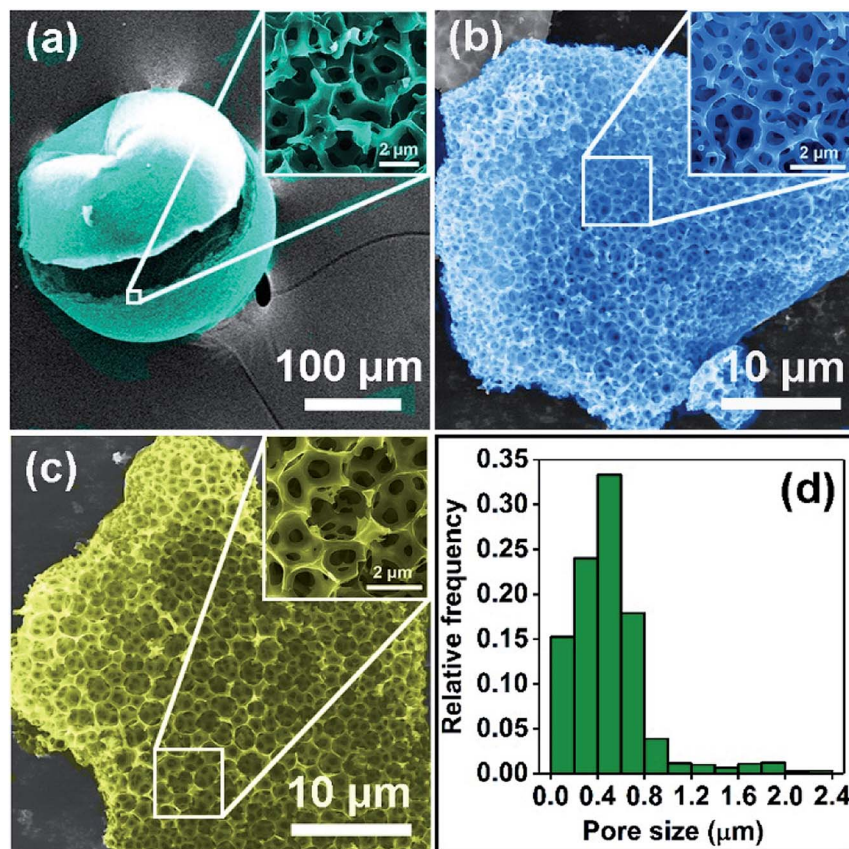

Fig. 1 FESEM images of (a) BSES, (b) C-700, and (c) HPC-1; (d) pore-size distribution of HPC-1.
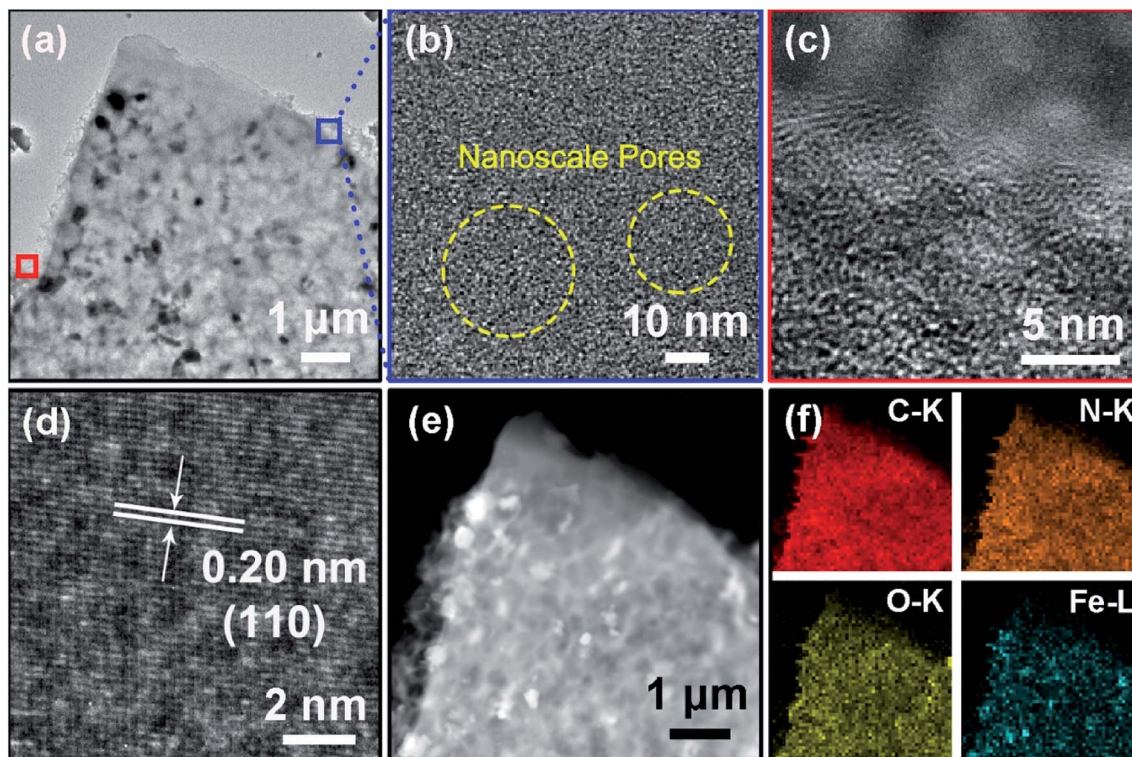
Fig. 2 TEM images of (a) HPC-1, (b) carbon skeleton; and HRTEM images of (c) carbon edge (corresponding to the left square area in (a)), and (d) Fe nanoparticles; (e) STEM image of (a); (f) EDS element mappings of C, N, O, and Fe elements.

indexed to the planes of (1 0 0), (1 0 1), and (1 1 2) for SiO_2, respectively. In addition, the peaks located at $29.4°$ and $39.4°$ are assigned to the planes of (1 0 4) and (1 1 3) for $CaCO_3$. After carbonization, the sample C-700 shows a broad peak at approximately $23°$ corresponding to amorphous carbon (Fig. S4b†). At the same time, the disappearance of the weak signals for $CaCO_3$ can be attributed to the pyrogenic decomposition of $CaCO_3$ at high temperature and the subsequent acid leaching. Fig. 3a displays the XRD patterns of HPCs. It can be noticed that SiO_2 phase vanishes after activation process due to the chemical reaction between SiO_2 and melting KOH during pyrolysis, which can be expressed using the chemical equation $SiO_2 + 2KOH \rightarrow K_2SiO_3 + H_2O$. Interestingly, the distinct diffraction peaks at $44.6°$, $65.0°$, and $82.3°$ for them can be well indexed to (1 1 0), (2 0 0), and (2 1 1) crystal planes of α-Fe with a body centered cubic (bcc) structure, respectively, with result in well accordance with the finding in HRTEM. In addition, it is noticed that the degree of crystallinity of α-Fe gradually enhanced accompanying with the increasing dosage of KOH. The origin of α-Fe crystals can be ascribed to the *in situ* reduction of native iron element in BSES to Fe crystals by the H_2 gas generated from the reaction between carbon and KOH during high-temperature reductive activation process,[28] which can be described as:

$$6KOH + 2C \rightarrow 2K + 2K_2CO_3 + 3H_2$$

$$Fe^{3+}/Fe^{2+} + H_2 \rightarrow Fe$$
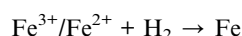
In addition, small amount of Fe_3C impurity is also detected in HPCs. Notably, the hump at approximately $2\theta = 23°$ corresponding to the amorphous carbon shifts to $26.5°$ in the case of HPC-2, which is indexed to crystal graphite (0 0 2) plane. Referring to the previous studies,[29] KOH is not instrumental in facilitating the graphitization of carbon, therefore, this phenomenon should be attributed to the fact that the generated α-Fe accentuated the graphitization of carbon due to its catalysis effect.[30] It is well-established that Fe is an ideal graphitization catalyst because there are only six electrons in its d-shell orbital and accepting electrons from carbon has small effect on energy level of this configuration, which enable Fe to form strong chemical bonds with carbon.[31] Furthermore, the presence of Si, Ca and Fe elements in BSES were confirmed by ICP-AES measurement, as exhibited in Fig. S5.† It is also found that BSES also contain K and Na elements apart from those elements detected by XRD. In the experimental process, these soluble sodium salts and potassium salts are easily removed by repeated wash with the deionized water.

To further validate the enhanced graphitization degree of HPCs, Raman spectroscopy was carried out to determine the C atom bonding state of samples. As shown in Fig. 3b, there are two peaks at approximately 1353 cm^{-1} and approximately 1595 cm^{-1} assigned to D and G bands for all the samples in the Raman spectra, respectively. The D band is related to the respiratory vibration of the sp^2 carbon atoms of A_{1g} mode, which results from the loss of the lattice symmetry, corresponding to the situation of symmetry breaking such as
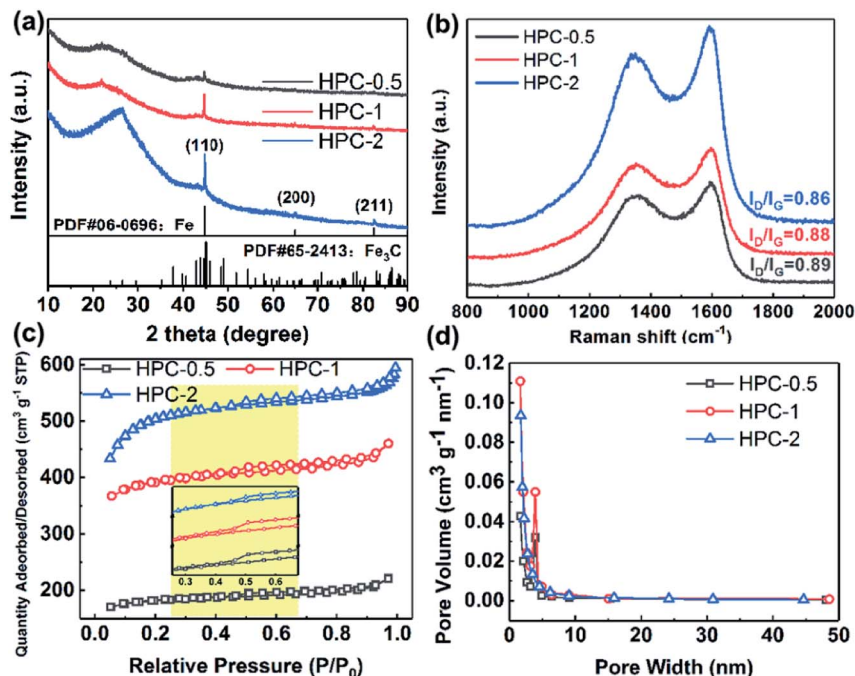
Fig. 3   (a) XRD patterns, (b) Raman spectrum, (c) nitrogen adsorption–desorption isotherms (the inset is the magnified isotherms of the yellow shaded part), and (d) pore-size distribution of HPCs.

presence of vacancies or substitutional heteroatoms. The G band arises from the E_{2g} optical phonon mode which is associated with in-plane sp^2 bond stretching of C atoms and occurs at all sp^2 sites.[32,33] Therefore, the value of the intensity of D band *versus* the intensity of G band (I_D/I_G) is usually introduced as a parameter to evaluate the degree of disorder of carbon materials. The I_D/I_G values for HPC-0.5, HPC-1, and HPC-2 are calculated to be 0.89, 0.88, and 0.86, respectively, demonstrating their moderate graphitization degree. In comparison with the value of I_D/I_G for C-700 (0.92, Fig. S6a†), the gradually decreasing values of I_D/I_G imply that the graphitization degree of HPCs is steadily enhanced as the relative amount of KOH increases. Combined with the preceding XRD analysis, it's reasonable to suppose that the increasing KOH promotes the reaction between carbon and KOH, and more Fe nanoparticles are reduced from the innate iron element, which strengthens the effect of catalyzing the graphitization of carbon.

Nitrogen adsorption–desorption analysis was further applied to characterize the porous structure of samples, and the specific surface area and pore size distribution were computed *via* Brunauer–Emmett–Teller (BET) method and Barrett–Joyner–Halenda (BJH) method, respectively. As displayed in Fig. S6b and c,† C-700 shows a typical type-IV isotherm with a type H4 hysteresis loop according to International Union of Pure and Applied Chemistry (IUPAC) classification, which could be ascribed to capillary condensation caused by the existence of abundant mesopores. The slight rising stage of isotherm at relative pressure (P/P_0) of 0.00–0.03 manifests the presence of small quantities of micropores, which could be evidenced by the specific surface area of 73.43 m^2 g^{-1} and the major pore size within the range of 1.2–147.6 nm. In comparison, HPCs exhibit

similar isotherms with type H4 hysteresis loops, however, their major pore size distribution ranges from 1.6 to 4.9 nm, which corresponds to micropores and mesopores (Fig. 3c and d). In addition, the isotherms of HPCs display almost horizontal plateaus at relatively lower P/P_0, indicating the presence of narrow slit-like pores containing some microporosity in the as-prepared HPCs.[34] Moreover, there is a steady increasing of specific surface area values in the order of 553.6 m^2 g^{-1} for HPC-0.5, 1192.0 m^2 g^{-1} for HPC-1, and 1886.16 m^2 g^{-1} for HPC-2. The considerably enhanced specific surface area values further demonstrate that a large number of micro/meso-porous structures were produced inside the carbon matrix, which is mainly ascribed to the etching of carbon and gas evolution,[30] as discussed before. In comparison with C-700, the ratios of micropore surface area (S_{Micro}) *versus* BET surface area (S_{BET}) and total pore volume (V_{Total}) *versus* micropore volume of HPCs are both dramatically increased (Table S1†), suggesting that KOH activation prefers the formation of micropores, which agrees with the reported literature.[28]

XPS was used to investigate the surface elemental compositions and chemical forms of samples. The fitted high-resolution XPS spectra of elements were obtained by using Gaussian–Lorentzian distribution based on Shirley type background correction. As shown in Fig. 4a, the peaks located at 284.8 eV, 285.9 eV and 288.4 eV in the deconvolution of C 1s spectrum corresponds to the C–C/C=C, C–N and O–C=O, respectively.[35,36] For N 1s, the original high-resolution XPS spectrum was deconvoluted into three peaks, assigned to pyridinic N (398.8 eV, N connected to two sp^2 hybridized C atoms), pyrrolic N (400.0 eV, N of a five-membered heterocyclic ring bonded with two C atoms), and graphitic N (401.2 eV, N bonded
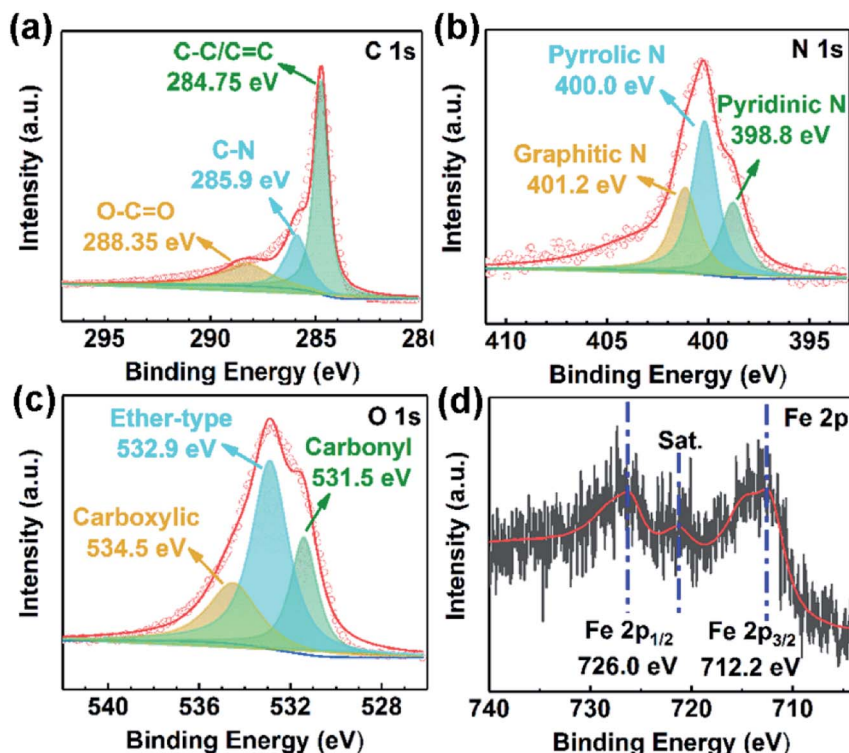
Fig. 4 XPS survey spectra of (a) C 1s, (b) N 1s, (c) O 1s, and (d) Fe 2p.

with three sp^2 hybridized C atoms), as shown in Fig. 4b.[37–39] The N atoms in HPCs disclose the presence of defects from atomic arrangement such as vacancies and bonding disorders. However, only pyridinic N and pyrrolic N can be considered structural defects that can serve as polarization centers because the formation of them is accompanied with loss of carbon atoms of the graphene layer. In addition, the peaks at 531.5 eV, 532.9 eV and 534.5 eV in O 1s spectrum are indexed to carbonyl, ether-type and carboxylic,[40,41] respectively, as exhibited in Fig. 4c. The presence of the large amount of nitrogen atoms (4.3 at%) and oxygen-containing functional groups are advantageous to increase the density of polarization centers of the materials.[42] Additionally, due to the low content of iron element at the surface of HPCs, the XPS signal from Fe presents a very weak intensity, as shown in Fig. 4d. As such, various measurements manifest that heteroatoms doped HPC/Fe composites have been successfully prepared.

To evaluate the microwave absorbing properties of samples, the electromagnetic parameters including relative complex permittivity $(\varepsilon_r = \varepsilon_r' - j\varepsilon_r'')$ and relative complex permeability $(\mu_r = \mu_r' - j\mu_r'')$ are studied as a function of dosage of KOH. Generally, it's believed that the real parts ε_r' and μ_r' are correlated to the ability of storing electronic energy and magnetic energy for absorbers, respectively; whereas the imaginary parts ε_r'' and μ_r'' are associated with the capacity for attenuating electronic energy and magnetic energy, respectively.[43,44] As shown in Fig. 5a, all of HPCs present higher ε_r' than the sample C-700 (Fig. S7a†). The ε_r' values of HPC-0.5, HPC-1, and HPC-2 drop from 12.2 to 9.4, from 18.0 to 11.7, and from 21.5 to 12.2 over

the frequency range of 2.0–18.0 GHz, respectively. This typical frequency dispersion behavior (ε_r' values decrease with the increasing frequency) is because the lag of dipole polarization strengthens upon the increasing frequency, which actually favors attenuating electromagnetic wave. Meanwhile, it is worth noting that the curves of ε_r' exhibit a stable ascending tendency with the increasing KOH amount. According to the Maxwell-Garnett theory, the porous materials composed of air and solid component, which theoretically belong to a type of composite, can be regarded as effective medium. The effective permittivity of these materials could be characterized by the following equation:[45,46]

$$\varepsilon_{\text{eff}}^{\text{MG}} = \left[\frac{(\varepsilon_2 + 2\varepsilon_1) + 2f_r(\varepsilon_2 - \varepsilon_1)}{(\varepsilon_2 + 2\varepsilon_1) - f_r(\varepsilon_2 - \varepsilon_1)} \right] \varepsilon_1 \quad (1)$$

where ε_1 is the permittivity of solid component, ε_2 is the permittivity of air, and f_r is the volume fraction of air in the effective media. It can be deduced from the eqn (1) that effective permittivity should decrease as the value of f_r increases. Moreover, the value of ε_r is mainly affected by the polarization capacity and the electrical conductivity of the materials according to the Debye theory and free electron theory. Also, it is noticed that the amplified values of ε_r' and ε_r'' for all the HPCs are all well agreed with the results of Raman spectrum and nitrogen adsorption and desorption analysis. Therefore, it can be supposed that the increasement of ε_r' values should be attributable to the enhanced polarization relaxation and conductive loss of samples.[29] With the increasing dosage of KOH, more carbon matrix was etched during the activation process, by
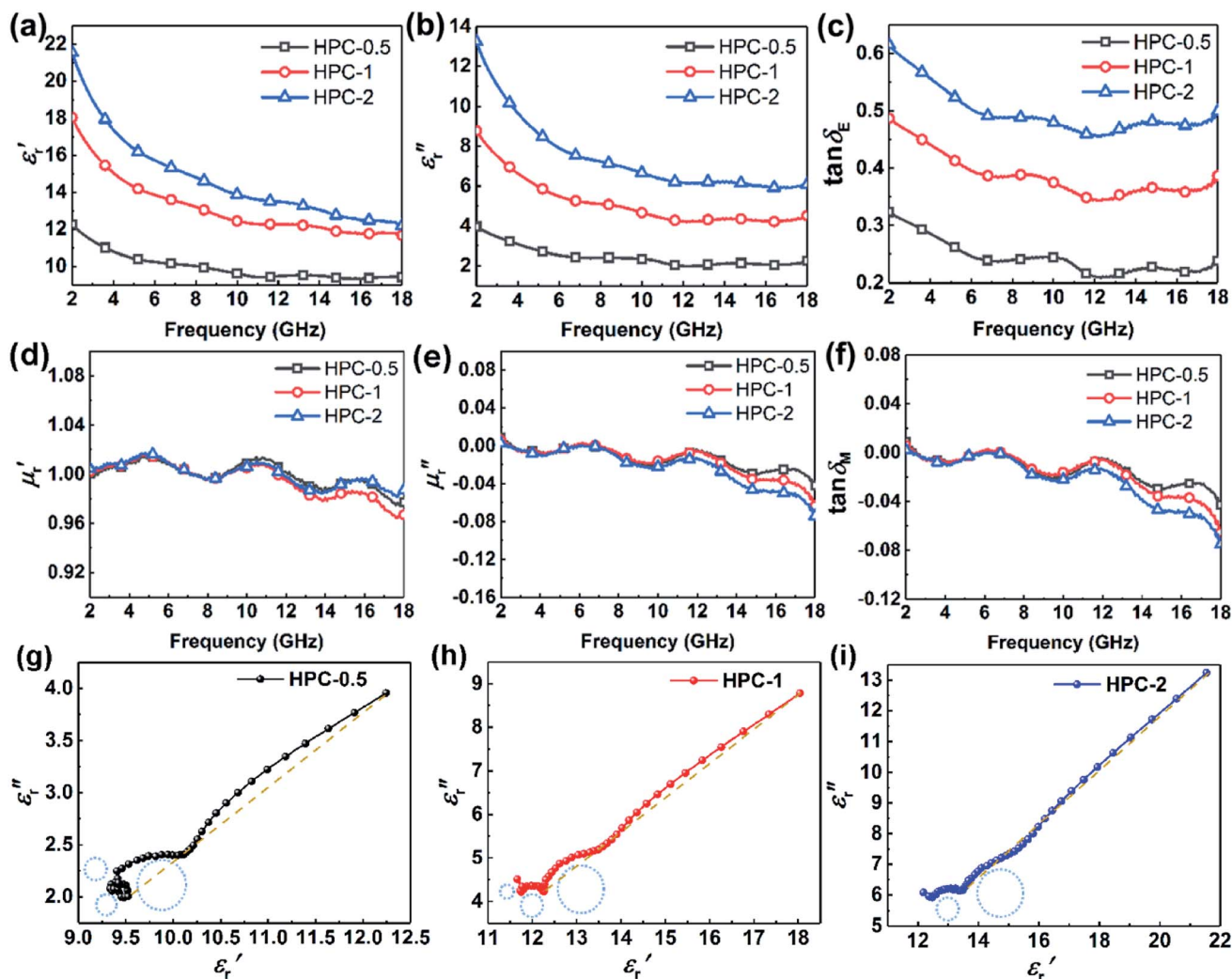
Fig. 5 Frequency dependence of (a) real part, (b) imaginary part of relative complex permittivity, and (c) tan δ_E; (d) real part, and (e) imaginary part of relative complex permeability, and (f) tan δ_M for HPCs; Cole–Cole curves of (g) HPC-0.5, (h) HPC-1, and (i) HPC-2.

which more gases were produced and the formation of micro/meso-porous structures in the carbon framework was promoted.[28] According to the Maxwell–Wagner effect, the charges will gather at the heterogeneous interfaces between two different materials and form cluster of large dipoles under irradiation of electromagnetic wave. Hence these numerous pores render the materials a great quantity of solid–air interfaces at which charges accumulate, which induces intense interfacial polarization. One must not overlook the fact that the Fe nanoparticles embedded in the carbon matrix endow the materials with abundant heterogeneous solid–solid interfaces, which gives rise to a stronger interfacial polarization loss.[47] In general, the Debye relaxation theory $(\varepsilon_r' - \varepsilon_\infty)^2 + (\varepsilon_r'')^2 = (\varepsilon_s - \varepsilon_\infty)^2$, *i.e.*, Cole–Cole semicircle, is employed to investigate the polarization behavior modes in the materials,[48] in which ε_s is static dielectric constant, and ε_∞ is dielectric constant at infinite frequency. A Cole–Cole hemicycle represents one Debye relaxation process. For respective Cole–Cole curves of HPC-0.5, HPC-1, and HPC-2 (Fig. 5g–i), three, three

and two distorted semicircles can be clearly observed, respectively, suggesting that there are other polarization modes aside from interfacial polarization relaxation occurring in the as-prepared HPCs. As confirmed by XPS, there were three bonding configurations of the N atoms in the as-prepared HPCs (pyridinic N, pyrrolic N and graphitic N), indicating that the N element inherited from chitosan and protein rearrange their bonding configurations, doping in the carbons and thus disrupting their ideal sp^2 hybridization. Nonetheless, only pyridinic N and pyrrolic N rearrange their bonding configurations with forming structural defects during pyrolysis, while graphitic N take place of the carbon atoms of the graphene nanosheets without producing defects. This can be understood by the fact that pyridinic N and pyrrolic N are bonded with two carbon atoms and graphitic N is connected to three carbon atoms. These structural defects and oxygen-containing functional groups can act as polar centers to stimulate dipole polarization.[23,49] When exposed to alternating electromagnetic field, electric dipoles induced by the N and O atoms that possess

higher electronegativity than C atom rotate repeatedly during the relaxation process, which will result in considerable energy loss. Moreover, the generated porous carbon skeleton which could be considered interconnected conductive network can convert the energy of alternating electromagnetic wave into thermal energy by microcurrent that involves the electron migration along carbon fabric and electron transfer between Fe nanoparticles and carbon medium,[50] inducing conductive loss. Compared with C-700 (Fig. S7c†), the conductive loss of HPCs is enhanced considerably, which is confirmed by the long tails of the Cole–Cole curves for HPCs.[51] It is noteworthy that HPC-2 presents a much straighter Cole–Cole curve with less semi-circles than other samples, which implies its stronger conductive loss and may be ascribed to its higher graphitization degree. The greater the graphitization degree is, the stronger conductive loss would be induced. The ε_r'' values for HPC-0.5, HPC-1, and HPC-2 drop from 4.0 to 2.3, from 8.8 to 4.5, and from 13.2 to 6.1 over the measured frequency range, respectively (Fig. 5b). The values of ε_r'' are proportional to the usage amount of KOH because of the ever-enhancing polarization ability of samples. Additionally, the unique layered porous architecture of HPC is immensely helpful in promoting the multiple reflection of microwave between particles due to the geometrical effect. The complicated structure of HPCs endows the material with more

active sites for reflection, ensuring more contact opportunities between electromagnetic wave and absorber. The transmitted microwave inside the HPCs could change its direction of propagation at the active sites and keep propagating forward, which extends its transmission paths largely and bringing about more intense dielectric loss. In general, the dielectric loss ability of absorber is estimated by the dielectric loss tangent ($\tan \delta_E = \varepsilon_r''/\varepsilon_r'$),[52] as displayed in Fig. 5c. The distinct peaks on $\tan \delta_E$ curves further provide evidence for the existence of multiple dielectric loss behaviors.

The frequency dependence of relative complex permeability is exhibited in Fig. 5d–f. In specific, the curves of μ_r' and μ_r'' and $\tan \delta_M$ for samples fluctuate at approximately 1.0 and approximately 0.0 over the measured frequency range, which is similar to those of C-700 (Fig. S7b†), demonstrating that the magnetic loss capacity of the samples could be essentially neglected. As discussed before, the Fe nanoparticles embedded in the carbon matrix bring benefits to reinforce the dielectric loss ability, they nonetheless have little contribution to induce magnetic loss because the content of Fe is not enough to generate considerable magnetic response when being in the alternating electromagnetic field. It is worth mentioning that the negative μ_r'' is related to the radiation of magnetic field. According to the Maxwell equations, the ac electric field can induce an internal
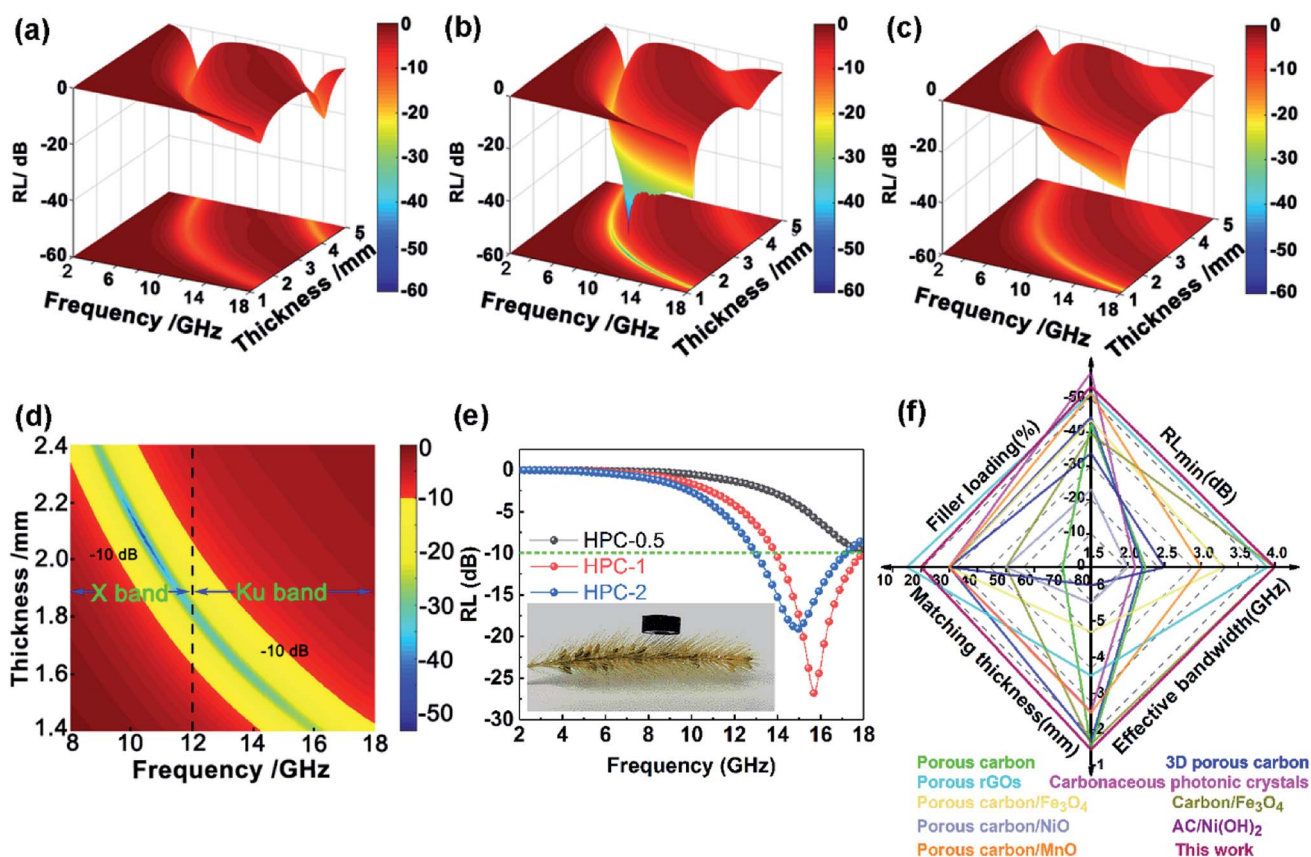

Fig. 6 Three-dimensional maps of RL for (a) HPC-0.5, (b) HPC-1, and (c) HPC-2; (d) two-dimensional contour of effective absorption bandwidth within 1.4–2.4 mm for HPC-1; (e) frequency dependence of RLs of HPCs at a thickness of 1.43 mm (the inserted optical image showing a ring-like sample (HPC-1) on a bristle grass); (f) comparison of the microwave absorption properties of HPC-1 with the recently reported bio-derived absorber.

magnetic field due to the motion of charges along the conductive mediums. In turn, the generated magnetic field can be radiated out from HPCs and transferred into electric energy. For HPCs, the counteraction between intrinsic magnetic loss and radiation of magnetic field is not balanced over the Ku band because of the low content of Fe, which results in the negative μ_r''. Therefore, it is believable that dielectric loss plays an overwhelmingly dominant role in attenuating electromagnetic waves in the as-prepared HPCs.

To further investigate the microwave absorbing properties of the samples, the reflection loss of samples is calculated *via* the following equation according to transmission line theory:[53]

$$RL = 20 \log \left| \frac{(Z_{in} - Z_0)}{(Z_{in} + Z_0)} \right| \quad (2)$$

$$Z_{in} = Z_0 \sqrt{\frac{\mu_r}{\varepsilon_r}} \tanh \left[\frac{j2\pi ft}{c} \sqrt{\mu_r \varepsilon_r} \right] \quad (3)$$

where Z_{in} and Z_0 are the input impedance at the absorber surface and the impedance of air, respectively, t is the thickness of absorber, and c represents the velocity of light. For describing the microwave absorbing properties of the samples more intuitively, the three-dimensional performance sketches with changing thickness and frequency were plotted, as illustrated in Fig. 6a–c. A qualified microwave absorber is required to possess a minimum RL (RL_{min}) less than −10 dB, which means the absorptivity beyond 90%. As shown in Fig. S7d,† C-700 displays poor microwave absorbing performance. By contrast, the microwave absorbing properties of HPCs are enhanced drastically. The results indicate that HPC-1 presents a RL_{min} of −53.6 dB at 10.4 GHz, and a wide effective absorption bandwidth of 14.56 GHz (3.44–18 GHz) with the thickness of 1.0–5.0 mm, covering the whole C (4–8 GHz), X (8–12 GHz) and Ku (12–18 GHz) bands. Notably, when the thickness is adjusted between only 1.4 and 2.4 mm, the effective bandwidth of HPC-1 can cover the whole X and Ku bands, as illustrated in Fig. 6d. When tuning the thickness to 1.43 mm, the RL_{min} is −26.8 dB at 15.7 GHz with an effective absorption bandwidth from 13.96 to 17.96 GHz (Fig. 6e). In addition, due to the highly porous characteristic of the as-prepared HPCs, the absorbers exhibit a compelling low-weight superiority. It can be seen from the inset in Fig. 6e that the ring-like sample made from HPC-1 can rest on the bristle grass without deforming the pubescence. In

comparison with the recently reported bio-derived MAMs, the HPC-1 prepared in this study exhibits a comparable or much better comprehensive property, as illustrated in Fig. 6f (the concrete values are listed in Table. S2†).

The excellent performance of HPCs is associated with the enhanced attenuation capability, which can reflect the extent to which the electromagnetic energy is consumed inside the material. In general, the total attenuation capability is featured by the attenuation constant (α) of absorbers as follows:[54]

$$\alpha = \frac{\sqrt{2}\pi f}{c} \sqrt{(\mu''\varepsilon'' - \mu'\varepsilon') + \sqrt{(\mu''\varepsilon'' - \mu'\varepsilon')^2 + (\mu'\varepsilon'' - \mu''\varepsilon')^2}} \quad (4)$$

As displayed in Fig. 7a, the α values present a monotonic rising trend upon the increasing dosage of KOH. In addition, HPC-1 and HPC-2 exhibit higher α values than C-700 (Fig. S7e†), demonstrating their stronger loss ability. As discussed before, the generated abundant micro/meso-porous structures, enhanced graphitization degree and Fe nanoparticles are responsible for the enhanced attenuation capability. However, the microwave absorbing performance of HPC-2 is inferior, even it displays higher α values. To obtain MAMs with outstanding performance, there is a crucial prerequisite, namely, well-matched characteristic impendence, that must be satisfied. A well-matched characteristic impendence means that electromagnetic wave is able to propagate into the interior of the material by the greatest extent with little reflection or without reflection at the air-material surfaces. Thanks to the positive balance between complex permittivity and permeability, HPC-1 had a better impedance matching and consequently exhibited more excellent performance than the other samples. Additionally, the values of relative input impedance $|Z_{in}/Z_0|$ of samples were computed *via* eqn (3) and are exhibited in Fig. 7b and S7f.† The closer the $|Z_{in}/Z_0|$ value is to 1.0, the better the matching between free space impedance and input impedance of absorber is. As seen, HPC-1 presents the optimum impedance matching in X band, while the other samples exhibit poor impedance matching with $|Z_{in}/Z_0|$ values higher or lower than 1.0, which further demonstrates the good impedance matching of HPC-1. Moreover, as discussed before, the porosity and graphitization degree of HPCs are both linearly ascending with the increasing dosage of KOH. The enhanced porosity is
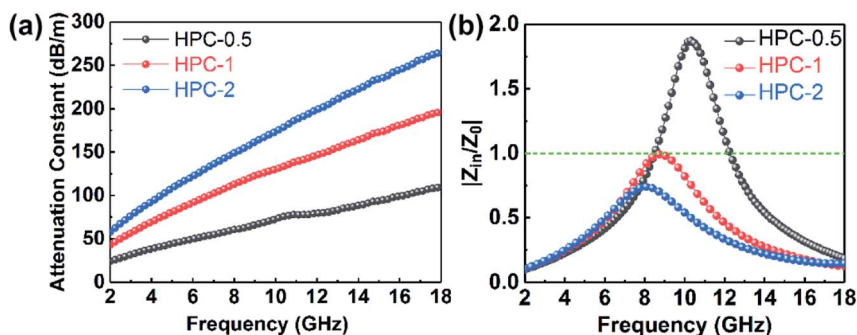

Fig. 7   (a) Attenuation factor, (b) relative input impedance $|Z_{in}/Z_0|$ of HPCs.
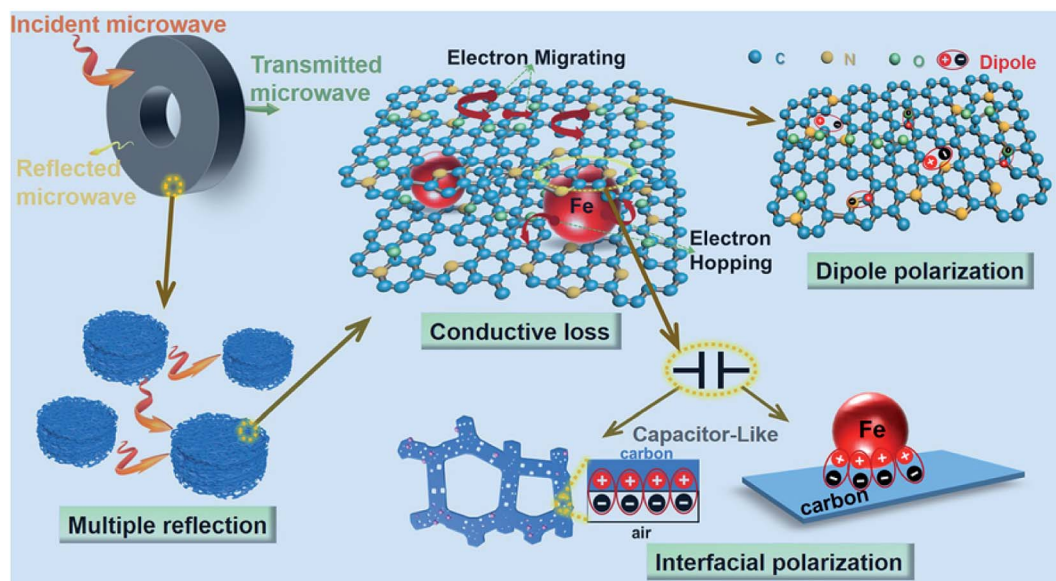
Fig. 8 Schematic illustration for electromagnetic wave absorption mechanisms exiting in HPCs.

advantageous to make the characteristic impedance of the material close or even equal to the free space; whereas an over-high graphitization degree could lead to a strong reflection of electromagnetic wave at the air–HPC interfaces. Due to the synergistic effect between porosity and graphitization degree, it is believable that the impedance matching of HPC-1 is well modulated because the balance of porosity and graphitization degree is realized by it. Substantially, the outstanding properties of HPC-1 can be attributed to the intense dielectric loss, which mainly stems from interfacial polarization at carbon–air and carbon–Fe interfaces, dipole polarization in heteroatoms-doped carbon matrix, microcurrent along carbon skeleton and Fe nanoparticles and multiple reflection of microwave among carbon particles, as summarized in Fig. 8.

4. Conclusions

In this work, natural iron embedded HPCs were successfully fabricated *via* a facile pyrolysis and subsequent reductive activation with KOH method. The Fe nanoparticles reduced from the natural iron element brought great benefits on interfacial polarization and conductive loss of the material. By modulating the dosage of KOH, the porosity and graphitization degree of HPCs could be tuned simultaneously, hence the impedance matching can be well regulated. When the relative mass ratio of KOH is 1, the sample displays RL_{min} of -53.6 dB at 10.4 GHz with a filler loading of 20%, and an effective absorption bandwidth covering the whole X and Ku bands with the thickness of 1.4–2.4 mm. In summary, these excellent properties can be mainly ascribed to the abundant multiscale porous structures (*i.e.*, micropores, mesopores and submicron/micron-scale pores), intense interfacial/dipole polarization loss, conductive loss and good impedance matching. This work provides insights on utilizing the bio-precursor rich in iron to prepare promising microwave absorber candidates with thin thickness

and high efficiency, and may promote the diversified development of bio-derived materials towards a more facile and gentler direction.

Conflicts of interest

The authors declare that there is no conflict of interest.

Acknowledgements

References

1 M. S. Cao, X. X. Wang, W. Q. Cao and J. Yuan, *J. Mater. Chem. C*, 2015, **3**, 6589–6599.
2 X. H. Qu, Y. L. Zhou, X. Y. Li, M. Javid, F. R. Huang, X. F. Zhang, X. L. Dong and Z. D. Zhang, *Inorg. Chem. Front.*, 2020, **7**, 1148.
3 Z. J. Li, H. Lin, S. Q. Ding, H. L. Ling, T. Wang, Z. Q. Miao, M. Zhang, A. L. Meng and Q. D. Li, *Carbon*, 2020, **167**, 148–159.
4 F. Qin and C. Brosseau, *J. Appl. Phys.*, 2012, **111**, 061301.
5 G. H. He, Y. P. Duan and H. F. Pang, *Nano-Micro Lett.*, 2020, **12**, 57.
6 Y. Zhang, Y. Huang, T. F. Zhang, H. C. Chang, P. S. Xiao, H. H. Chen, Z. Y. Huang and Y. S. Chen, *Adv. Mater.*, 2015, **27**, 2049.
7 B. Wen, M. S. Cao, M. M. Lu, W. Q. Cao, H. L. Shi, J. Liu, X. X. Wang, H. B. Jin, X. Y. Fang, W. Z. Wang and J. Yuan, *Adv. Mater.*, 2014, **26**, 3484.

8 M. K. Han, X. W. Yin, L. Kong, M. Li, W. Y. Duan, L. T. Zhang and L. F. Cheng, *J. Mater. Chem. A*, 2014, **2**, 16403.

9 Y. Ra'di, C. R. Simovski and S. A. Tretyakov, *Phys. Rev. Appl.*, 2015, **3**, 037001.

10 Y. C. Du, T. Liu, B. Yu, H. B. Gao, P. Xu, J. Y. Wang, X. H. Wang and X. J. Han, *Mater. Chem. Phys.*, 2012, **135**, 884.

11 D. Micheli, A. Vricella, R. Pastore and M. Marchetti, *Carbon*, 2014, **77**, 756.

12 H. Sun, R. C. Che, X. You, Y. S. Jiang, Z. B. Yang, J. Deng, L. B. Qiu and H. S. Peng, *Adv. Mater.*, 2014, **26**, 8120.

13 Y. Zhang, Y. Huang, H. H. Chen, Z. Y. Huang, Y. Yang, P. S. Xiao, Y. Zhou and Y. S. Chen, *Carbon*, 2016, **105**, 438.

14 H. L. Xu, X. W. Yin, M. Zhu, M. K. Han, Z. X. Hou, X. L. Li, L. T. Zhang and L. F. Cheng, *ACS Appl. Mater. Interfaces*, 2017, **9**, 6332.

15 Y. X. Huang, Y. Wang, Z. M. Li, Z. Yang, C. H. Shen and C. C. He, *J. Phys. Chem. C*, 2014, **118**, 26027.

16 Z. C. Wu, W. Hu, T. Huang, P. Lan, K. Tian, F. F. Xie and L. Li, *J. Mater. Chem. C*, 2018, **6**, 8839.

17 H. Q. Zhao, Y. Cheng, W. Liu, L. Yang, B. S. Zhang, L. P. Wang, G. B. Ji and Z. J. Xu, *Nano-Micro Lett.*, 2019, **11**, 24.

18 S. Dutta, A. Bhaumik and K. C.-W. Wu, *Energy Environ. Sci.*, 2014, **7**, 3574.

19 Q. X. Yang, W. T. Yang, Y. Y. Shi, L. J. Yu, X. Li, L. M. Yu, Y. B. Dong, Y. F. Zhu and Y. Q. Fu, *J. Mater. Sci.: Mater. Electron.*, 2019, **30**, 1374.

20 J. B. Xi, E. Z. Zhou, Y. J. Liu, W. W. Gao, J. Ying, Z. C. Chen and C. Gao, *Carbon*, 2017, **124**, 492.

21 S. T. Liu, X. G. Chen, A. B. Zhang, K. K. Yan and Y. Ye, *BioResources*, 2014, **9**, 2328.

22 X. Qiu, L. X. Wang, H. L. Zhu, Y. K. Guan and Q. T. Zhang, *Nanoscale*, 2017, **9**, 7408.

23 X. F. Zhou, Z. R. Jia, A. L. Feng, X. X. Wang, J. J. Liu, M. Zhang, H. J. Cao and G. L. Wu, *Carbon*, 2019, **152**, 827.

24 Z. C. Wu, K. Tian, T. Huang, W. Hu, F. F. Xie, J. J. Wang, M. X. Su and L. Li, *ACS Appl. Mater. Interfaces*, 2018, **10**, 11108.

25 L. H. Wang, H. T. Guan, J. Q. Hu, Q. Huang, C. J. Dong, W. Qian and Y. D. Wang, *J. Alloys Compd.*, 2019, **803**, 1119–1126.

26 X. W. Chen, O. Timpe, S. B. A. Hamid, R. Schlögl and D. S. Su, *Carbon*, 2009, **47**, 340–343.

27 Z. H. Wang, D. K. Shen, C. F. Wu and S. Gu, *Green Chem.*, 2018, **20**, 5031–5057.

28 J. C. Wang and S. Kaskel, *J. Mater. Chem.*, 2012, **22**, 23710.

29 H. Q. Zhao, Y. Cheng, H. L. Lv, G. B. Ji and Y. W. Du, *Carbon*, 2019, **142**, 245–253.

30 Y. N. Gong, D. L. Li, C. Z. Luo, Q. Fu and C. X. Pan, *Green Chem.*, 2017, **19**, 4132–4140.

31 A. Ōya and H. Marsh, *J. Mater. Sci.*, 1982, **17**, 309–322.

32 S. K. Singh, H. Prakash, M. J. Akhtar and K. K. Kar, *ACS Sustainable Chem. Eng.*, 2018, **6**, 5381–5393.

33 L. Saini, M. K. Patra, M. K. Dhaka, R. K. Jani, G. K. Gupta, A. Dixit and S. R. Vadera, *CrystEngComm*, 2018, **20**, 4630–4640.

34 S. Ghosh, R. Das and M. K. Naskar, *J. Am. Ceram. Soc.*, 2016, **99**, 2273–2282.

35 B. K. Mutuma, C. I. Garcia-Martinez, R. C. Dias, B. J. Matsoso, N. J. Coville and I. A. Hümmelgen, *New J. Chem.*, 2019, **43**, 8418–8427.

36 J. Feng, F. Z. Pu, Z. B. Li, X. H. Li, X. Y. Hu and J. T. Bai, *Carbon*, 2016, **104**, 214–225.

37 D. H. Guo, R. Shibuya, C. Akiba, S. Saji, T. Kondo and J. Nakamura, *Science*, 2016, **351**, 361–365.

38 Z. Y. Sui, Y. N. Meng, P. W. Xiao, Z. Q. Zhao, Z. X. Wei and B. H. Han, *ACS Appl. Mater. Interfaces*, 2015, **7**, 1431–1438.

39 P. Chen, L. K. Wang, G. Wang, M. R. Gao, J. Ge, W. J. Yuan, Y. H. Shen, A. J. Xie and S. H. Yu, *Energy Environ. Sci.*, 2014, **7**, 4095–4103.

40 J. Li, K. Liu, X. Gao, B. Yao, K. F. Huo, Y. L. Cheng, X. F. Cheng, D. C. Chen, B. Wang, W. M. Sun, D. Ding, M. L. Liu and L. Huang, *ACS Appl. Mater. Interfaces*, 2015, **7**, 24622–24628.

41 J. Ding, H. L. Wang, Z. Li, K. Cui, D. S. Karpuzov, X. H. Tan, A. Kohandehghan and D. Mitlin, *Energy Environ. Sci.*, 2015, **8**, 941–955.

42 X. L. Zheng, J. Feng, Y. Zong, H. Miao, X. Y. Hu, J. T. Bai and X. H. Li, *J. Mater. Chem. C*, 2015, **3**, 4452–4463.

43 X. Yang, Y. P. Duan, Y. S. Zeng, H. F. Pang, G. J. Ma and X. H. Dai, *J. Mater. Chem. C*, 2020, **8**, 1583–1590.

44 H. X. Zhang, Z. R. Jia, A. L. Feng, Z. H. Zhou, C. H. Zhang, K. K. Wang, N. Liu and G. L. Wu, *Compos. Commun.*, 2020, **19**, 42–50.

45 L. X. Wang, P. P. Zhou, Y. Guo, J. Zhang, X. Qiu, Y. K. Guan, M. X. Yu, H. L. Zhu and Q. T. Zhang, *RSC Adv.*, 2019, **9**, 9718–9728.

46 B. Zhao, X. Zhang, J. S. Deng, Z. Y. Bai, L. Y. Liang, Y. Li and R. Zhang, *Phys. Chem. Chem. Phys.*, 2018, **20**, 28623–28633.

47 H. L. Xu, X. W. Yin, Z. C. Li, C. L. Liu, Z. Y. Wang, M. H. Li, L. T. Zhang and L. F. Cheng, *Nanotechnology*, 2018, **29**, 184003.

48 L. Wang, Y. Huang, X. Ding, P. B. Liu, M. Zong and Y. Wang, *Mater. Sci. Eng., B*, 2013, **178**, 1403–1409.

49 L. Huang, J. J. Li, Z. J. Wang, Y. B. Li, X. D. He and Y. Yuan, *Carbon*, 2019, **143**, 507–516.

50 X. C. Zhao, Z. M. Zhang, L. Y. Wang, K. Xi, Q. Q. Cao, D. H. Wang, Y. Yang and Y. W. Du, *Sci. Rep.*, 2013, **3**, 3421.

51 H. Q. Zhao, Y. Chen, H. L. Lv, B. S. Zhang, G. B. Ji and Y. W. Du, *ACS Sustainable Chem. Eng.*, 2018, **6**, 15850–15857.

52 J. Liu, Y. P. Duan, L. L. Song, J. J. Hu and Y. S. Zeng, *Compos. Sci. Technol.*, 2019, **182**, 107780.

53 L. L. Song, Y. P. Duan, J. Liu and H. F. Pang, *Nano Res.*, 2020, **13**, 95–104.

54 W. H. Gu, J. Zheng, X. H. Liang, X. Q. Cui, J. B. Chen, Z. Zhang and G. B. Ji, *Inorg. Chem. Front.*, 2020, **7**, 1667.